European Conference on Computational Fluid Dynamics
ECCOMAS CFD 2006
P. Wesseling, E. Oñate and J. Périaux (Eds)
© TU Delft, The Netherlands, 2006

3D PARALLEL SPECTRAL COMPUTATIONS OF FAN NOISE

Farzad Taghaddosi* **and Wagdi G. Habashi†**

*CFD Lab., Dept. of Mechanical Engineering, McGill University,
Montreal, QC H3A 2S6, Canada
e-mail: farzad@cfdlab.mcgill.ca

†Director, CFD Lab., Dept. of Mechanical Engineering, McGill University,
Montreal, QC H3A 2S6, Canada
e-mail: wagdi.habashi@mcgill.ca

Key words: Fan Noise, Aeroacoustics, Spectral Element Method, Schur Complement Method, Parallel Computing

Abstract. *A three-dimensional computational aeroacoustics code has been developed for the simulation of tone noise generated by turbofan engine inlets. The code is based on the linearized Euler equations, rewritten in terms of acoustic potential and solved in the frequency domain. Spatial discretization is performed using a spectral element method.*

Solution of the linear system of equations is based on the Schur complement method, which is solved using a matrix-free iterative method on multi-processors. A new preconditioner, which acts locally on individual subdomains, has been introduced to accelerate the convergence. Moreover, mathematical formulations are presented for implementation of geometric symmetry conditions for general, nonsymmetric wave propagation to further reduce computational cost associated with these types of problems.

Numerical results include acoustic propagation from a uniform cylinder as a validation test case and a generic scarfed inlet with close to 2 million grid points, both solved using from 8-48 processors. The code is demonstrated to be robust and efficient in simulating ducted acoustic propagation.

1 INTRODUCTION

In modern turbofan engines with a large bypass ratio, fan noise dominates the engine noise signature during take-off and landing. The noise, which is caused by the rotor-stator interaction, propagates with the blade-passage frequency (BPF) or its harmonics.

Generally, two different approaches are used in numerically analyzing fan noise problem. One is based on computational aeroacoustics (CAA), where the computational domain covers the fan face, inlet duct, and a truncated region in front of the duct's exit, representing the far-field. Noise generation at the rotor is modeled using either the Tyler & Sofrin theory[20], or by directly calculating pressure variations using first

principles[2,19]. To avoid any dissipation or dispersion associated with numerical modeling of the governing equations, high-order schemes must be used for both spatial and temporal discretizations[8,17].The second approach is based on the acoustic analogy, where the near-field (encompassing the acoustic source and duct interior) is resolved using the Euler or Navier-Stokes equations, and linear acoustic theory in the form of an integral solution is applied at the far-field[10,12].

2 PROBLEM FORMULATION

The work presented in this paper is based on a full flow-field CAA analysis. The governing equations are the continuity and momentum equations, in the presence of a mean flow, which are further simplified by introducing a potential, Φ^*, such that $\vec{V}^* = \nabla\Phi^*$. Using this assumption, the governing equations become

$$\frac{\partial \rho^*}{\partial t^*} + \nabla \cdot (\rho^* \nabla \Phi^*) = 0, \tag{1}$$

$$\rho^* = \left[1 - (\gamma - 1)\left(\frac{\partial \Phi^*}{\partial t^*} + \frac{\nabla\Phi^* \cdot \nabla\Phi^* - M_\infty^2}{2}\right)\right]^{1/(\gamma-1)}, \tag{2}$$

in which ρ^* is the density, M_∞ is the freestream Mach number, and γ is the ratio of specific heats. The equations are non-dimensionalized using the freestream speed of sound, c_∞, density, ρ_0, and fan radius, R, as reference variables. Equations (1) and (2) are further simplified using a small perturbation assumption, where flow variables are considered to be superposition of an acoustic perturbation on the mean value, i.e., $\rho^* = \rho_0 + \rho$ and $\Phi^* = \Phi_0 + \Phi$. Incorporating these assumptions in the above leads to the linearized form of the continuity and momentum equations, respectively,

$$\frac{\partial \rho}{\partial t} + \nabla \cdot (\rho_0 \nabla\Phi + \rho \nabla\Phi_0) = 0, \tag{3}$$

$$\rho = -\frac{\rho_0}{c_0^2}\left[\frac{\partial \Phi}{\partial t} + (\nabla\Phi_0 \cdot \nabla\Phi)\right], \tag{4}$$

in which subscript '0' denotes mean values.

For the purpose of discretization, the weak form is built using the method of weighted residuals applied to the continuity equation

$$\int_\Omega \left[\frac{\partial \rho}{\partial t} + \nabla \cdot (\rho_0 \nabla\Phi + \rho \nabla\Phi_0)\right] \Psi \, d\Omega = 0, \tag{5}$$

with Ψ being the test function. Applying the divergence theorem and the proper vector identity, the weak form becomes

$$\int_\Omega \left[\Psi \frac{\partial \rho}{\partial t} - \nabla\Psi \cdot (\rho_0 \nabla\Phi + \rho \nabla\Phi_0)\right] d\Omega = -\int_\Gamma \Psi(\rho_0 \nabla\Phi + \rho \nabla\Phi_0) \cdot \vec{n} \, d\Gamma, \tag{6}$$

in which Γ indicates the boundary of the computational domain, Ω. Due to time-harmonic nature of the fan noise problem, the acoustic potential is assumed to be of the form

$$\Phi = \phi(x, y, z)\, e^{-i\bar{\omega}t}, \tag{7}$$

were, $\bar{\omega}$ is the reduced frequency, $\bar{\omega} = \omega R/c_\infty$, and $i = \sqrt{-1}$. This means that the solution to the acoustic problem will be sought in the frequency domain. Similarly, the test function is defined as

$$\Psi = \psi(x, y, z)\, e^{i\bar{\omega}t}, \tag{8}$$

consistent with the definition of the dot product in the complex Hilbert space. Using these definitions and equation (4), the weak form reduces to

$$\begin{aligned}\int_\Omega \frac{\rho_0}{c_0^2}\Big[\,&\bar{\omega}^2\phi\psi + (u_0^2 - c_0^2)\,\phi_x\psi_x + (v_0^2 - c_0^2)\,\phi_y\psi_y + (w_0^2 - c_0^2)\,\phi_z\psi_z + \\ &u_0v_0\,(\phi_x\psi_y + \phi_y\psi_x) + u_0w_0\,(\phi_x\psi_z + \phi_z\psi_x) + v_0w_0\,(\phi_y\psi_z + \phi_z\psi_y) + \\ &i\bar{\omega}u_0\,(\phi\psi_x - \phi_x\psi) + i\bar{\omega}v_0\,(\phi\psi_y - \phi_y\psi) + i\bar{\omega}w_0\,(\phi\psi_z - \phi_z\psi)\Big]\, d\Omega = \\ &-\int_\Gamma \Psi(\rho_0\nabla\Phi + \rho\nabla\Phi_0)\cdot\vec{n}\; d\Gamma,\end{aligned} \tag{9}$$

in which $\nabla = (\partial_x, \partial_y, \partial_z)$, and $(u_0, v_0, w_0) = \nabla\Phi_0$ are mean flow velocity components.

Spatial discretization of the weak form is based on subdivision of the computational domain into hexahedral elements over which a spectral approximation based on a tensor product of N^{th}-degree shape functions is used[13]. The shape functions or interpolating polynomials, $h_i(\xi)$, are collocated at Gauss-Chebyshev-Lobatto points, defined as $\xi_i = -\cos \pi i/N, i = 0, \ldots, N$. Using the discrete orthogonality properties of the Chebyshev polynomials, $T_n(\xi) = \cos(n\, \cos^{-1}\xi)$, the shape functions are[5],

$$h_m(\xi) = \frac{2}{Nc_m}\sum_{n=0}^{N}\frac{1}{c_n}\,T_n(\xi_m)\,T_n(\xi), \tag{10}$$

where $c_0 = c_N = 2$ and $c_n = 1$ otherwise. Hexahedral elements in the physical space are transformed into the bicuboid reference element, $\mathcal{Q} = [-1, +1]^3$, using the affine transformation

$$\mathbf{x}(\xi, \eta, \zeta) = \sum_{i=0}^{N}\sum_{j=0}^{N}\sum_{k=0}^{N} h_i(\xi)\, h_j(\eta)\, h_k(\zeta)\, (x, y, z)^e_{ijk}. \tag{11}$$

Similarly, for the acoustic potential, $\phi(x, y, z)^e$, using an isoparametric formulation, we have

$$\phi(\xi,\eta,\zeta) = \sum_{i=0}^{N}\sum_{j=0}^{N}\sum_{k=0}^{N} h_i(\xi)\, h_j(\eta)\, h_k(\zeta)\, \phi^e_{ijk}, \tag{12}$$

with the test function defined as

$$\psi = h_l(\xi)\, h_m(\eta)\, h_n(\zeta). \tag{13}$$

Using the above spectral approximation, the integrals in (9) can be evaluated either numerically or analytically, resulting in a system of linear equations in terms of the acoustic potential, $A\phi = f$. The solution to this system, which provides the acoustic field, is discussed later.

3 BOUNDARY CONDITIONS

In the acoustic problem, three different types of boundaries exist: solid surfaces, acoustic source, and the far-field.

For a typical turbofan engine, solid surfaces include the inner duct, possibly a centerbody, and the nacelle. Since the flow is considered inviscid, only a no-penetration condition is applied on all solid surfaces. That is,

$$\begin{cases} \nabla\Phi \cdot \vec{n} = 0 \\ \nabla\Phi_0 \cdot \vec{n} = 0 \end{cases} \quad \text{on } \Gamma_w, \tag{14}$$

where $\vec{n}$ is the outward normal vector to the solid boundary, Γ_w. This boundary condition is applied by simply discarding the contour integral on the right-hand side of equation (9) because it will be identically zero at such boundaries.

At the acoustic source, which is considered to be at a uniform section of the fan inlet with a circular cross section, the boundary conditions are imposed by specifying the acoustic potential,

$$\Phi(x,r,\theta) = \sum_{s} A_s J_m(k_{ms} r)\, e^{i(k_x x + m\theta)}, \tag{15}$$

in which m and s are the order of circumferential and radial modes, respectively, J_m is the Bessel function of the first kind and of order m, k_{ms} is the eigenvalue corresponding to (m,s) mode, A_s is the amplitude of the s^{th} radial mode, r is the radial distance, and θ is the azimuthal angle[14]. For an annular acoustic source, i.e., when the centerbody is present, the potential at the source is specified as follows

$$\Phi(x,r,\theta) = \sum_{s} \left[A_s J_m(k_{ms} r) + Y_m(k_{ms} r)\right] e^{i(k_x x + m\theta)}, \tag{16}$$

in which Y_m is the Bessel function of the second kind and of order m.

The boundary conditions at the far-field, where the domain is truncated, are implemented through a damping region near the outflow boundary to avoid reflection of outgoing waves back into the computational domain. This is achieved by adding a term of the form $-\nu(x)\rho$ to the right-hand side of Eq. (3), in which $\nu(x)$ simulates exponential damping

$$\nu(x) = \nu_0 \left|(x - x_I)/D\right|^n . \tag{17}$$

Here, ν_0 is the damping amplitude, x_I the coordinate of the inner-edge of the damping layer, D is the thickness of the layer, and n the damping exponent.

The far-field boundary conditions are applied by modifying the weak form in the damping layer, where integrals of the form

$$-\int_\Omega (\nu\rho)\Psi \, d\Omega \; = \int_\Omega \frac{\nu\rho_0}{c_0^2} \left(i\bar{\omega}\phi\psi + u_0\phi_x\psi + v_0\phi_y\psi + w_0\phi_z\psi\right) d\Omega \tag{18}$$

are evaluated along each coordinate direction and their contribution are added to the element matrices. It should be pointed out that due to strong damping effects at the far-field boundaries, the contour integral in equation (9) will have negligible contribution to the solution at the far-field and therefore is neglected in all computations.

4 Geometric Symmetry

It is not uncommon for the nacelle or inlet duct to have a geometric symmetry, whether with respect to the xy-plane, xz-plane, or both (axisymmetry). So, one can properly take advantage of the symmetry conditions and perform calculations for only one-half or a quarter of the domain. This means a reduction of computational cost associated with building coefficient matrices by nearly a factor of 2 or 4, respectively. The cost associated with solving the system of equations will reduce even further because operation counts are nonlinear (exponential) functions of the number of equations, whether a direct or an iterative solver is used.

Removing part of the computational domain due to symmetry will expose the plane of symmetry as an exterior boundary, along which one should evaluate the boundary integral

$$-\int_\Gamma \Psi(\rho_0\nabla\Phi + \rho\nabla\Phi_0)\cdot\vec{n}\, d\Gamma, \tag{19}$$

according to the weak form (6). Figure 1 shows the front view of a circular duct symmetric with respect to the xy-plane, in which half the computational domain, e.g. $z < 0$, has been removed. Referring to this figure, details of implementation for this case are discussed below. Generalization to other cases of geometrical symmetry, e.g. with respect to the xz-plane, is straightforward.

Given that on a symmetry boundary the normal component of mean flow velocity is zero, the boundary integral in (19) reduces to

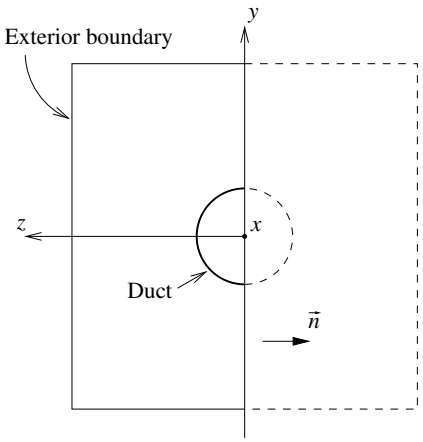

Figure 1: Front view of a duct in a symmetric domain.

$$I_{sym} = -\int_{\Gamma} \Psi \rho_0 (\nabla\Phi \cdot \vec{n})\, d\Gamma. \tag{20}$$

The integral in (20) is separated into two, one covering the area above the x-axis and the other the area below it, $I_{sym} = I_{sym})_{y>0} + I_{sym})_{y<0} = I^+_{sym} + I^-_{sym}$. The case of $y = 0$ may not always be present and is discussed later. We discuss the evaluation of I^+_{sym} only, with a similar procedure to follow for I^-_{sym}. In the derivations, the cylindrical form of the gradient operator is used along the plane of symmetry

$$\nabla = \frac{\partial}{\partial r}\,\vec{e}_r + \frac{1}{r}\frac{\partial}{\partial\theta}\,\vec{e}_\theta + \frac{\partial}{\partial x}\,\vec{e}_x, \tag{21}$$

where the polar angle θ is measured counter clockwise and relative to the y-axis[1].
► **Case:** $y > 0$. Along the positive side of the xy-plane, the normal vector is, $\vec{n} = -\vec{e}_\theta$. Therefore, $\nabla\Phi \cdot \vec{n} = -\frac{1}{r}\frac{\partial\Phi}{\partial\theta}$. Using the cylindrical form of acoustic potential along the plane of symmetry, $\Phi = \phi(x, r)\, e^{im\theta} e^{-i\omega t}$, one obtains

$$\nabla\Phi \cdot \vec{n} = -\frac{im}{r}\,\phi(x, r)\, e^{im\theta} e^{-i\omega t}. \tag{22}$$

Since, on the plane of symmetry and for $y > 0$, $\theta = 0$ and $r = y$, then,

$$\nabla\Phi \cdot \vec{n} = -\frac{im}{y}\,\phi(x, y)\, e^{-i\omega t}. \tag{23}$$

Similarly, defining the test function along the plane of symmetry to be $\Psi = \psi(x, y)\, e^{i\omega t}$, the boundary integral (20) becomes

[1]Note that this convention must match the one used for variation of θ when boundary conditions are applied on the acoustic source.

$$I^{+}_{sym} = im \int_{\Gamma^{+}} \Big(\frac{\rho_0}{y}\Big) \phi\psi \, d\Gamma. \tag{24}$$

This integral can be easily evaluated on the symmetry plane with its contribution added to corresponding nodes in the element coefficient matrix.

Note that the integral will be identically zero, if no azimuthal modes are propagated, i.e., $m = 0$. This is due to the fact that both plane wave or purely radial modes have radial symmetry.

► **Case:** $y = 0$. In evaluation of the integral (24), it was assumed that $y \neq 0$. That is, the possibility of having any points on the x-axis, which would make the integral singular was excluded. To resolve the singularity, numerical integration of boundary integrals involving such singular points can be performed at the points of a staggered grid based on Gauss-Chebyshev (GC) points instead of Gauss-Chebyshev-Lobatto (GCL) points.

The set of N Gauss-Chebyshev points are defined as

$$\hat{\sigma}_i = -\cos\Big[\frac{(2i+1)\pi}{2N}\Big], \qquad i = 0, \ldots, N-1, \tag{25}$$

where N is the number of GCL points used in the spectral grid, and the corresponding interpolation function collocated at N Gauss-Chebyshev points is[5]

$$\hat{h}_m(\sigma) = \frac{2}{N} \sum_{n=0}^{N-1} \frac{1}{\hat{c}_n} T_n(\hat{\sigma}_m) \, T_n(\sigma), \tag{26}$$

where $\hat{c}_0 = 2$ and $\hat{c}_n = 1$. Therefore, the boundary integral for faces with singular points can be evaluated as before, except that variables ρ_0 and y, and the Jacobian $|J|$ will be evaluated at the GC points.

It should be noted that any face on the plane of symmetry that intersects the x-axis may not necessarily have a GCL point on the axis itself. So, the singularity of integral in (24) (or I^{-}_{sym}) will depend on the shape of the grid on the plane of symmetry and the number of GCL points used.

5 SOLUTION METHOD

The system of equations obtained through discretization of the weak form, $A\phi = f$, is complex-valued, non-symmetric, and indefinite. Further, the coefficient matrix is known to be very ill-conditioned, a well-known characteristic of spectral methods. Given the large size of practical applications, which are of the order of $\mathcal{O}(10^5)$ and more, iterative methods are the method of choice due to their reduced cost, especially that coefficient matrices are extremely sparse.

However, it is well-known that classical iterative methods and also more advanced acceleration techniques (Krylov subspace methods) generally fail to converge for problems

based on spectral discretization, unless a very good preconditioner is used. Finding suitable preconditioners, however, is still an active research area with progress made mostly in the area of elliptic PDE's[18].

In the current paper, a non-overlapping domain decomposition technique, known as the Schur complement method, is used for the solution of the acoustic problem. This reduces solution of the original system of equations to that of the Schur system, which is usually more than one order of magnitude smaller and therefore easier and faster to solve. A parallel environment is used to perform all computations with the extensive use of MPI and PETSc libraries[1].

To build the Schur system, the computational domain is first divided into 'p' subdomains using ParMETIS[9], where 'p' is the number of processors. In each subdomain 'i', the elemental equations $A^{(i)}\phi^{(i)} = f^{(i)}$ are partitioned into a block form

$$A^{(i)} = \begin{bmatrix} A_{II}^{(i)} & A_{IB}^{(i)} \\ A_{BI}^{(i)} & A_{BB}^{(i)} \end{bmatrix}, \qquad \phi^{(i)} = \begin{Bmatrix} \phi_I \\ \phi_B \end{Bmatrix}, \qquad f^{(i)} = \begin{Bmatrix} f_I \\ f_B \end{Bmatrix}, \tag{27}$$

where $A_{II}^{(i)}$ is the submatrix containing contribution of interior nodes on each other, $A_{IB}^{(i)}$ the submatrix containing contribution of interior nodes on boundary nodes, and so on. Using the block matrices, one can obtain the Schur system for global boundary points, φ_B: $S\varphi_B = g$, in which the Schur matrix and the right-hand side are given by

$$S = \sum_{i=1}^{p} \tilde{R}_i^T S_i \tilde{R}_i, \qquad g = \sum_{i=1}^{p} \tilde{R}_i^T g^{(i)}. \tag{28}$$

Here, $S_i = A_{BB}^{(i)} - A_{BI}^{(i)} {A_{II}^{(i)}}^{-1} A_{IB}^{(i)}$ is the Schur complement for subdomain 'i', and $g^{(i)} = f_B^{(i)} - A_{BI}^{(i)} {A_{II}^{(i)}}^{-1} f_I^{(i)}, i = 1, \ldots, p$, is the associated right-hand side vector. The matrix $\tilde{R}_i$ is a Boolean operator which maps global boundary points at domain interfaces to boundary points on subdomain 'i'. Once the solution to the Schur system is obtained, i.e., unknowns at interface boundaries are evaluated, the solution within each subdomain can be calculated independently[16].

The Schur matrix, S, defined above is not usually constructed explicitly due to the high cost involving calculation of ${A_{II}^{(i)}}^{-1}$. Instead, the system is solved using a matrix-free approach. Since any iterative method requires only multiplication of S by a vector in their algorithm, this can be accomplished using Schur complement of individual subdomains using gather/scatter operations applied to the global vector.

5.1 Solver Analysis

Among different Krylov subspace methods, four different methods were tested for the solution of the Schur matrix: CGS, GMRES, TFQMR and Bi-CGSTAB. Other methods could not be used because they involve multiplication by the transpose of the Schur matrix, which in this case is not available since S is not formed explicitly.

Method	CGS	GMRES	TFQMR	Bi-CGSTAB
Solution Time (min:sec)	15:07	9:29	13:54	15:47
No. of Iterations	190	173	142	139

Table 1: Solution time and number of iterations for different algorithms.

For a typical test case (solution of the plane wave propagation from an unflanged cylinder) convergence history of the above four methods is compared in Figure 2. Table 1 gives the solution time and the corresponding iteration count for each method. The CGS, TFQMR, and Bi-CGSTAB take much longer to converge compared to the GMRES, since their algorithm involves 2 matrix-vector multiplications per iteration, as opposed to only one such operation for the GMRES. Also, it was found that the convergence history of both TFQMR and Bi-CGSTAB were very sensitive to round-off errors, producing different residual histories at different runs. So, given the monotonic convergence of the GMRES method and its lower solution time, it was considered to be the most suitable algorithm for solution of the acoustic problem and used for all calculations.

Theoretically, the full GMRES is guaranteed to converge in n iterations, n being the size of the coefficient matrix. However, due to cost considerations, the restarted version GMRES(m) is commonly used, with $m =$ generally having a value of 20-35. For non-positive definite problems (such as the acoustic problem), restarted GMRES could stagnate or lead to a very slow convergence[15]. This is shown in Figure 3 for the scarfed inlet test case.

As a result, the restart parameter was set to a large value ($m =$ 400-600) to assure optimal convergence. Using such a large value would obviously increase memory usage, but given the poor convergence rate associated with the smaller values, it would be a logical trade-off. Moreover, extra memory usage would not be extraordinarily high given that the size of the Schur matrix is of the order of $\mathcal{O}(10^5)$ for the largest test problem. Also, by comparison, the Schur complement method would require a much larger amount of memory.

5.2 Preconditioning

To speed up the convergence, a preconditioner is proposed for the solution of the Schur matrix, which is a modified version of the Neumann-Neumann preconditioner[11]. The modification is based on the observation that one can approximate S_i, which is expensive to evaluate, with the local matrix of interface boundary points, $A^{(i)}_{BB}$. The proposed preconditioner, therefore, becomes

$$M_P^{-1} = \sum_{i=1}^{p} \tilde{R}_i^T \tilde{D}_i \, {A^{(i)}_{BB}}^{-1} \tilde{D}_i \tilde{R}_i, \tag{29}$$

where $\tilde{D}_i$ is a diagonal weighting matrix whose components are the inverse of the number of subdomains the corresponding node in the matrix belongs to. The above preconditioner is easy to evaluate since it only involves a solution using $A^{(i)}_{BB}$, which is a relatively small

matrix, the size of the number of boundary points belonging to subdomain 'i'. Moreover, it is a local preconditioner applied on individual subdomains. As a result, interprocessor communications are minimized during the bulk of the preconditioning step.

For a sample problem, propagation of plane wave from a circular cylinder, tests were performed to demonstrate the performance of different preconditioners. The problem involved close to 220 000 unknowns, with the size of the Schur matrix about 16 000. The preconditioners tested were all using the global matrix of boundary points, $A_{BB} = \sum_{i=1}^{p} \tilde{R}_i^T A_{BB}^{(i)} \tilde{R}_i$, its approximation, $M_B^{-1} = {A_{BB}}^{-1}$, a Jacobi variant $M_J^{-1} = [\text{Diag}(A_{BB})]^{-1}$, and a diagonal probing preconditioner[3] involving A_{BB}. Figure 4 shows the convergence history. As expected, using the global boundary matrix (A_{BB}) provides the fastest convergence, followed by its less accurate approximations, M_P^{-1} and M_J^{-1}, respectively. However, referring to Table 2, it is clear that the proposed preconditioner is the best choice in terms of the solution time. It is also a good compromise between the simple Jacobi method M_J^{-1} and the more expensive M_B^{-1} preconditioner.

6 RESULTS AND DISCUSSION

The first test concerns radiation of the first azimuthal (spinning) mode, $(m, s) = (1,0)$ from a cylinder of zero thickness. This test also serves to demonstrate the validity of the theoretical development for the symmetry boundary conditions, as presented in § 4. Figure 5 shows the computational domain with dimensions of 7×14×10. The duct radius, R, is chosen to be one and the duct length is $2.5R$. The frequency at the source is 320.075 Hz, which is equivalent to a reduced (non-dimensional) frequency of $\bar{\omega} = 5.91$. The yellow surface indicates the plane of symmetry. Damping is applied on all external boundaries, except on the symmetry plane, with damping parameters set to $(D, \nu_0, n) = (2,\ 8,\ 2)$. There are a total of 2004 elements in the domain. Within each element, a fifth-order spectral approximation is used ($N = 5$), giving rise to a spectral grid with 263 816 nodes and a resolution of 6.4 points per wavelength (PPW) on average. Details of generating the spectral grid can be found in Reference[4].

The acoustic energy of the azimuthal modes peaks off the axis. This is shown in Figure 6, where far-field directivity is compared with analytical results and the boundary integral calculations of Lidoine *et al.*[10], showing a very good agreement both qualitatively and quantitatively. The test case was solved using 8 processors on an SGI Origin 3400 machine with 400MHz MIPS R12000 CPU's. Using the preconditioned Schur complement method and with a Schur matrix of size 18 685, it took about 14 minutes and 230 iterations to converge the residual below 10^{-10}. Due to the relatively high order of approximation used, the assembly time was relatively and about 33 minutes.

Preconditioner	None	M_J^{-1}	M_P^{-1}	M_B^{-1}
Solution Time (min:sec)	10:55	9:39	9:29	14:58
No. of Iterations	261	223	173	129

Table 2: Solution time and iteration count for different preconditioners.

The next test represents a practical example, where a generic scarfed inlet has been considered. Figure 7 shows the geometry of the scarfed inlet in which the lips have elliptical profiles. For numerical calculations, the exterior boundary is moved by one meter behind the fan face to create enough thickness for damping to be applied. The size of the computational domain is therefore 4.7×7.4×7.4 m, with a total of 15 328 elements. A close-up of the spectral grid on the inlet is shown in Figure 8.

The non-dimensional frequency is $\bar{\omega}$ =17, which is relatively high. Propagation of the (13,0) mode in the absence of the mean flow is considered. For this frequency and azimuthal mode, the cut-off ratio is $\xi_{13,0} = 1.138 > 1$, which indicates a propagating mode. A fifth-order approximation is used within each element ($N = 5$) equivalent to an approximate number of 7.77 points per wavelength. Given the relatively high frequency, a larger damping layer is used with damping parameters set to $(D, \nu_0, n) = (3,\ 10,\ 2)$. Figure 9 shows the acoustic pressure contours at the inlet (fan face), inside the nacelle and on its walls, and at a distance from the duct exit. Given the shape of the Bessel functions, for higher azimuthal modes the acoustic energy is convected closer to the walls. This is clearly visible by the shape of contour lines on the inlet face.

Directivity of the SPL has been measured at a distance of 5λ from the nacelle exit plane and plotted against the numerical results of Hamilton and Astley[6] in Figure 10. The method used in [6] is a hybrid approach, where quadratic finite elements are used in the near-field and 5^{th}-order infinite elements in the far-field. Referring to Figure 10, numerical values near the duct axis ($-20° \leq \theta \leq 20°$) are meaningless and would diminish if a higher order of approximation was used. Outside this region, however, there is little match between our results and those presented in [6]. To gain a better insight and to better judge the quality of results for the two numerical methods, analytical results corresponding to propagation from a zero-thickness uniform duct at the same frequency and azimuthal mode are plotted in the same figure. By comparison, the spectral method provides very smooth curves and "qualitatively" exhibits a similar trend as the exact solution. The results presented by Hamilton and Astley, on the other hand, are very oscillatory and only weakly resemble the exact data or the present calculation. However, it seems that both numerical methods predict the location of maximum SPL closely. Given the above argument, the accuracy of the method presented in [6] is questionable.

The effect of finite lip thickness is a reduction in the far-field SPL directivity, especially at large angles away from the duct axis. This explains the deviation in our results from the exact solution for $|\theta| > 70°$. Due to the extended lower lip, which shields part of the acoustic energy directed in that direction, there is an asymmetry in directivity curve, causing the maximum SPL to be about 4.5 dB less in the downward direction.

Computations for this test case were performed on 48 processors using the resources of the CLUMEQ Supercomputer Center. An SGI Origin 3800 machine with 400 MHz MIPS R12000 processors was used. The acoustic field contains a total of 1 969 746) equations. The time required for building the system of equations was about 44 minutes, while solution of the Schur matrix required 65 minutes to converge. The performance

of the proposed preconditioner is shown in Figure 11 for different number of partitions. The number of iterations range between 200 and 600, which is relatively low, given the ill-conditioning of the Schur system. The good convergence rate is indicative of the robustness and efficiency of the proposed method for such a large problem.

Finally, to show the parallel efficiency of the code, computation time for building and assembling the matrix vs. the number of processors is plotted in Figure 12. Given the extremely large size of the problem, it was not possible to run the test on a single CPU, as required in the definition of speedup formula. Instead, the 8-processor results were used as the reference data. The parallel performance is clearly very satisfactory, showing a *superlinear* speedup for the majority of the calculations. Such an excellent scaling is attributed to many factors, among which is the optimality of the algorithms used in the code and also an efficient memory management.

7 CONCLUSIONS

A parallel 3D code has been developed using the spectral element method for the simulation of noise generated by turbofan engine inlets. The applicability of the code, however, is not restricted to fan noise problems. The 3D formulation allows prediction of far-field acoustic radiation from a duct of an arbitrary (asymmetric) shape and geometry.

Solution of the linear system of equations is known to be very challenging due to the ill-conditioning of the coefficient matrix. Here, a non-overlapping domain decomposition technique, known as the Schur complement method, was used to solve the system of equations. The reason for adopting this approach was two fold: first, the Schur matrix is known to be better conditioned and denser than the original matrix, and second, its size is generally (depending on the number of domains) an order of magnitude less than the original system.

The reduced Schur system, however, was still difficult to solve and preconditioning was definitely an important requirement. The preconditioning proposed in this paper was constructed using local matrix of domain boundary points and was shown to yield very satisfactory results.

Given that Schur complement method is inherently an expensive method, both in terms of memory usage and the computational cost, a better preconditioning, or one built for the original system of equations would be desirable. Our work is currently focused on achieving this goal.

It should, however, be noted that for the foreseeable future a full CAA analysis for large domains remains a remote possibility. For such applications, hybrid techniques provide a suitable alternative.

ACKNOWLEDGMENTS

The authors would like to thank Pratt & Whitney Canada for their financial support during the initial stages of this research. This work was partially funded by the National

Sciences and Engineering Research Council of Canada (NSERC). Also, the help of the support staff of the CLUMEQ Supercomputing Center is greatly appreciated.

REFERENCES

[1] S. Balay, K. Buschelman, V. Eijkhout, W.D. Gropp, D. Kaushik, M.G. Knepley, L.C. McInnes, B.F. Smith, and H. Zhang, "PETSc Users Manual," *ANL-95/11 - Revision 2.1.5*, Argonne National Laboratory, 2004.

[2] R.T. Biedron, C.L. Rumsey, G.G. Podboy, and M.N. Dunn, "Predicting the Rotor-Stator Interaction Acoustics of a Ducted Fan Engine," *AIAA Paper 2001-0664*, 2001.

[3] T.F. Chan and D. Goovaerts, "Schur Complement Domain Decomposition Algorithms for Spectral Methods," *Applied Numerical Mathematics*, Vol. 6, pp. 53-64, 1989.

[4] M.O. Deville, P.F. Fischer, and E.H. Mund, *High-Order Methods for Incompressible Fluid Flow*, Cambridge University Press, 2002.

[5] G. Evans, *Practical Numerical Integration*, John Wiley & Sons, 1993.

[6] J.A. Hamilton and R.J. Astley, "Acoustic Propagation on Irrotational Mean Flows Using Transient Finite and Infinite Elements," *AIAA Journal*, Vol. 43, pp. 124-134, 2005.

[7] G.F. Homicz and J.A. Lordi, "A Note on Radiative Directivity Patterns of Duct Acoustic Modes," *Journal of Sound and Vibration*, Vol. 41, pp. 283-290, 1975.

[8] S.K. Lele, "Compact Finite Difference Schemes with Spectral-like Resolution," *Journal of Computational Physics*, Vol. 103, 16-42, 1992.

[9] G. Karypis, V. Kumar, and K. Schloegel, "Graph Partitioning for High-performance Scientific Simulations," *Computing Reviews*, Vol. 45, pp. 110, 2004.

[10] S. Lidoine, H. Batard, S. Troyes, A. Delnevo, and M. Roger, "Acoustic Radiation Modeling of Aeroengine Intake - Comparison between Analytical and Numerical Methods," *AIAA Paper 2001-2140*, 2001.

[11] J. Mandel, "Balancing Domain Decomposition," *Communications in Numerical Methods in Engineering*, Vol. 9, pp 233-241, 1993.

[12] Y. Özyörük and L.N. Long, "A Navier-Stokes/Kirchhoff Method for Noise Radiation from Ducted Fans," *AIAA Paper 94-0462*, 1994.

[13] A.T. Patera, "A Spectral Element Method for Fluid Dynamics: Laminar Flow in a Channel Expansion," *Journal of Computational Physics*, Vol. 54, pp. 468-488, 1984.

[14] I.D. Roy, W. Eversman, and H.D. Meyer, "Improved Finite Element Modeling of the Turbofan Engine Inlet Radiation Problem," *NASA-CR-204341*, 1993.

[15] Y. Saad, *Iterative Methods for Sparse Linear Systems*, SIAM Publications, 2003.

[16] B. Smith, P. Bjorstad, and W. Gropp, *Domain Decomposition: Parallel Multilevel Methods for Elliptic Partial Differential Equations*, Cambridge University Press, 1996.

[17] C.K.W. Tam and J.C. Webb, "Dispersion-Relation-Preserving Finite Difference Schemes for Computational Acoustics," *Journal of Computational Physics*, Vol. 107, pp. 262-281, 1993.

[18] A. Toselli and O. Widlund, *Domain Decomposition Methods - Algorithms and Theory*, Springer Series in Computational Mathematics, Vol. 34, 2005.

[19] N. Tsuchiya, Y. Nakamura, A. Yamagata, and H. Kodama, "Fan Noise Prediction Using Unsteady CFD Analysis," *AIAA Paper 2002-2491*, 2002.

[20] J.M. Tyler and T.G. Sofrin, "Axial Flow Compressor Noise Studies," *SAE Transactions*, Vol. 70, pp. 309-332, 1962.

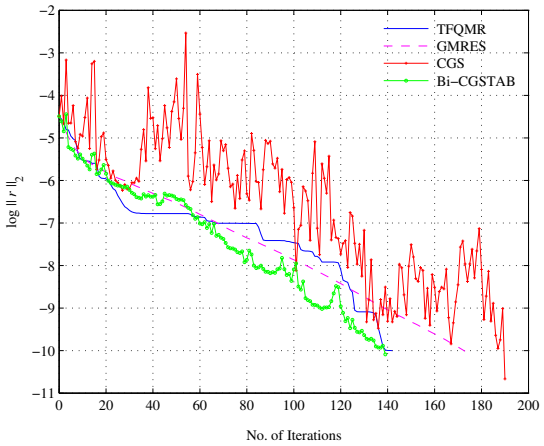

Figure 2: Convergence behavior of the Schur matrix using different iterative solvers.

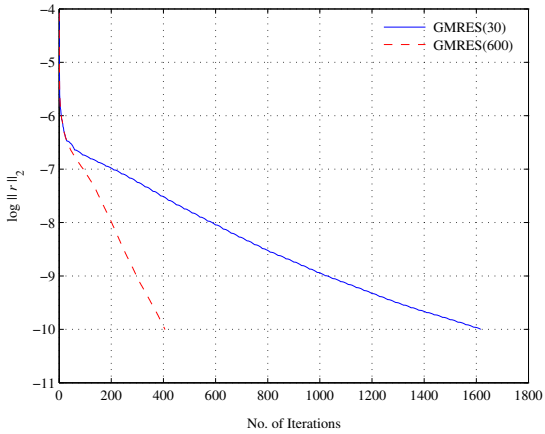

Figure 3: Effect of the restart parameter on convergence rate of the GMRES algorithm.

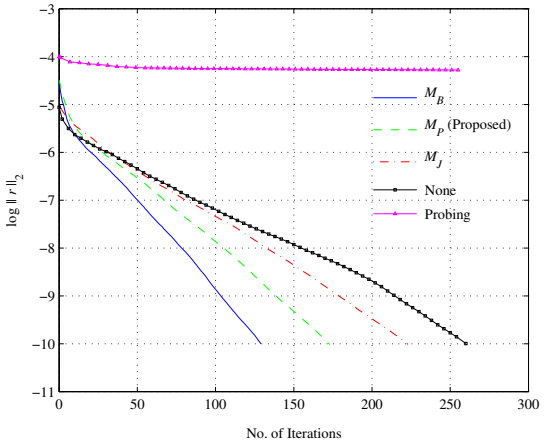

Figure 4: Effect of different preconditioners on convergence history of the Schur matrix using the GMRES solver.

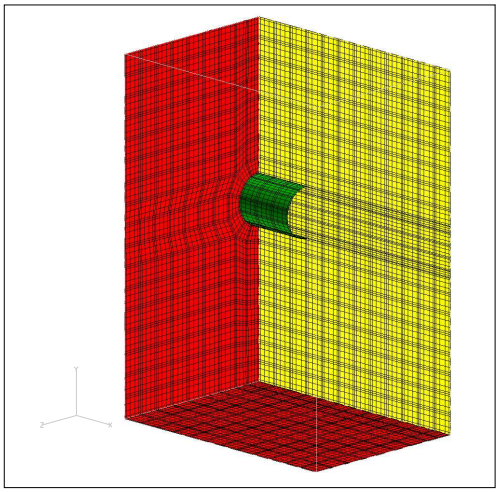

Figure 5: Computational domain and spectral grid outline for the first azimuthal mode calculations.

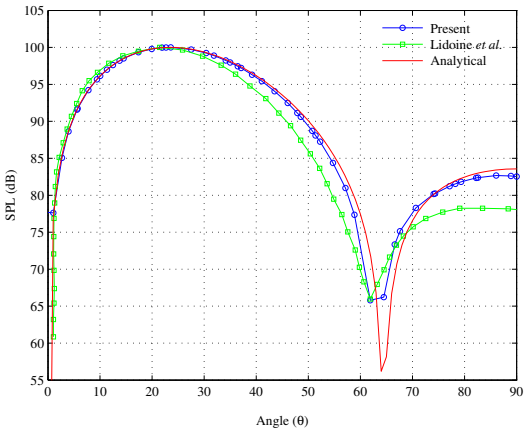

Figure 6: Directivity at the far-field for the first azimuthal mode.

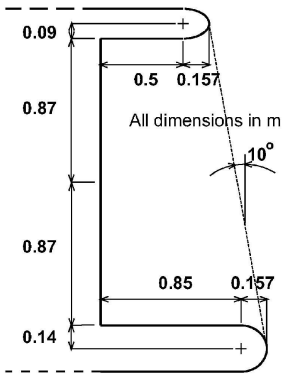

Figure 7: Geometry of the scarfed inlet.

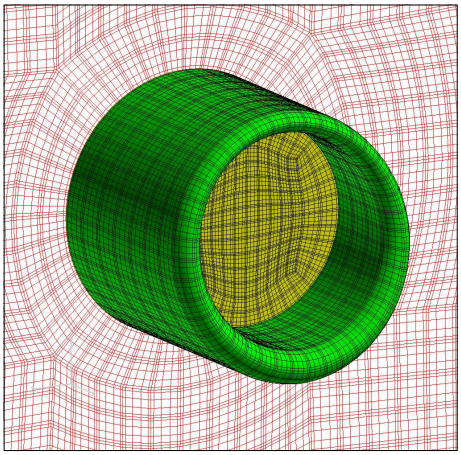

Figure 8: Outline of the spectral mesh in and around the nacelle.

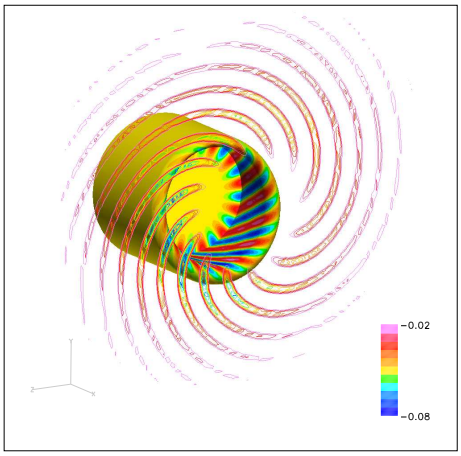

Figure 9: Acoustic pressure contours inside the nacelle and at an axial location away from the inlet.

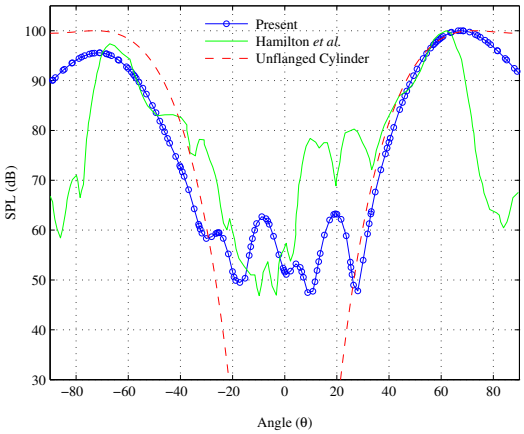

Figure 10: Directivity of the SPL for the (13,0) mode on the xy-plane; $\bar{\omega} = 17$.

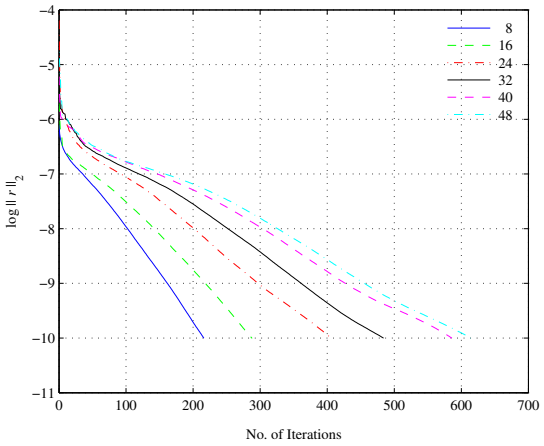

Figure 11: Effect of the number of partitions on the convergence rate of the Schur matrix.

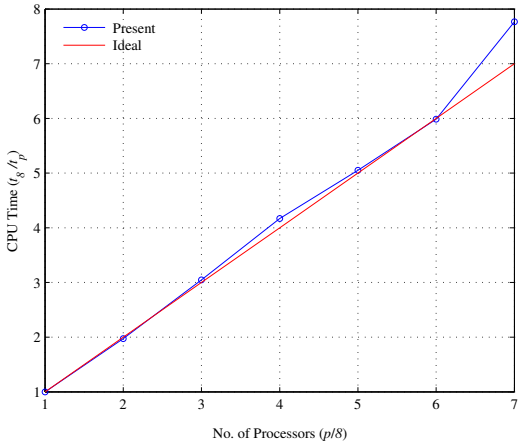

Figure 12: Speedup vs. number of CPU's; data normalized with respect to $p = 8$.